ADVANCES IN MATERIALS SCIENCE, Vol. 22, No. 3 (73), September 2022

DOI: 10.2478/adms-2022-0013

Chakkravarthi Rajarajan[1*], Tushar Sonar[2], Paramasivam Sivaraj[3], Selvaraj Raja[4], Nallusamy Mathiazhagan[5]

[1,5]Department of Mechanical Engineering, Meenakshi Ramaswamy Engineering College, Thathanur 621804, Tamil Nadu, India

[2] Department of Mechanical Engineering, G. S. Mandal's Maharashtra Institute of Technology, Aurangabad 431010, Maharashtra, India

[3]Centre for Materials Joining and Research (CEMAJOR), Department of Manufacturing Engineering, Annamalai University, Annamalai Nagar 608 002, Tamil Nadu, India

[4]Central Library, Alagppa University, Karaikudi 630 003, Tamil Nadu, India

***** *rajachozhan93@gmail.com*

THE EFFECT OF RESISTANCE SPOT WELDING PARAMETERS ON MICROSTRUCTURE AND STRENGTH OF DP800 STEEL JOINTS USING RESPONSE SURFACE METHODOLOGY

ABSTRACT

The main objective of this paper is to analyze the direct and interaction effect of resistance spot welding (RSW) parameters on microstructure and strength of DP800 steel joints using response surface methodology (RSM). The DP800 steel sheets were spot welded in straight lap and cross lap joint configuration using RSW. The relationship between the RSW parameters, tensile shear fracture load (TSFL) and nugget zone hardness (NZH) was established employing statistical regression analysis and validated using Analysis of Variance (ANOVA). The DP800 steel joints made using welding current of 5.0 kA, electrode pressure of 4.0 MPa, and welding time of 1.50 s displayed maximum STRAIGHT-TSFL of 21.7 kN, CROSS-TSFL of 17.65 kN, and NZH of 589 $HV_{0.5}$ respectively.

Keywords: *Resistance spot welding; DP800 steel; tensile shear fracture load; weld nugget; microstructure; hardness; optimization; response surface methodology*

INTRODUCTION

Dual-phase 800 (DP800) steel is advanced high-strength steel (AHSS) consisting of a 50% soft ferrite matrix and 50% hard martensite phase [1]. It leads to many advantages such as a high work hardening rate, ductility, and superior strength. It proves their applicability as lightweight high strength material for electric vehicle structural applications [2]. This improves fuel efficiency, mileage and crashworthiness. It also lowers vehicle weight and exhaust gas. It is employed in the fabrication of structural frames and doors in trucks and light passenger vehicles. They are offering a promising approach in manufacturing next-generation lightweight vehicles [3]. The joining of DP800 steel by fusion welding is challenging owing to its high strength and complicated microstructural phases. Due to the high heat input, it causes issues in welding such

as softening in HAZ and solidification cracking [4]. When the DP800 steel is heated to the tempering temperature during fusion welding, its softness primarily owing to the transformation of existing hard martensite into soft tempered martensite and carbides precipitation. This significantly degrades the strength performance of DP steel joints [5]. Hence it finds less suitability for joining DP steel in fabrication of structural frames for electric vehicles. In this study, resistance spot welding (RSW) is employed to join DP800 steel to fabricate spot joints of superior performance. It entails resistive heating of joining surfaces at a temperature below the melting point of metal and under pressure. This significantly minimizes the problems in joining DP800 steel such as HAZ softening and solidification cracking [6]. Each vehicle contains nearly 10,000 spot welds. It is economical, shop friendly and provides a high production rate. Compared to fusion welding processes, it can be easily automated and maintained [7]. To assess the quality of spot joints, nugget diameter is determined and tensile shear strength (TSS) of spot joints is evaluated. The microstructure and TSS of nugget areas are influenced by RSW parameters such as welding current, welding time, and electrode force [8-10]. Hence parameter optimization in RSW is crucial aspect to maximize the performance of welded joints.

Kishore et al. [11] analyzed the effect of spot welding current on strength of galvanized DP-600 steel sheets and found significant enhancement in strength of joints for increase in welding current up to 9 kA. Aydin and Ertan [12] studied the effects of RSW parameters in joining DP600 steel and found that higher level of welding current and time enhanced tensile strength and hardness due to the evolution of lath martensite in NZ. Janardhan et al. [13] investigated the prestraining effect on fatigure and load carrying strength in RSW of DP-600 steel sheets and found that at increased levels of prestrain, the load carrying strength of spot joints was improved. The prestraining levels extend significant effect on high cycle fatigure life of joint. Kishore et al. [14] studied the influcen of spot welding current on strength and nugget diameter of Zn coated DP and interstitial free steel and reported that the strength and nugget diameter of joints increases at increased levels of welding up to the evolution of expuilsion. Sevim [15] investigated fracture toughness of galvanized DP450 steel spot joints and concluded that the fracture toughness of spot joints depends on the diameter of nugget, thickness of sheet, tensile force of rupture, hardness and ratios of nucleus size. Yaghoobi et al. [16] investigated RSW of DP and IF steel and reported that the TSFL of spot joints increased at increased levels of weldig current along with increase in nugget diameter. Javheri et al. [17] analzed the mechanical performance of RSW spot joints of DP1000 steel and found that the strength of spot joints and the dislocation velocity for reaching the higher value of strain hardening was enhanced after RSW. Elitas and Demir [18] evaluated the induced residual stress in RSW of DP600 steel and found compressive stress in the specimen. The joint welded using welding current of 5 kA and 6 bar electrode pressure revealed higher residual stress level. Marwan and Kacer [19] optimized RSW parameters for making dissimilar spot joints of DP600 steel and TRIP800 steel. Elitas [20] studied the effect of RSW parameters on tensile strength and fracture behavior of DP1200 steel spot joints and found that expulsion extends detrimental effects on tensile shear strength of spot joints. Onal and Kaya [21] optimized RSW paraemters using Taguchi method for joining Al-Si coated 22MnB5 sheets. Cavdar et al. [22] investigated the effect of RSW parameters on surface morphology of AISI304 steel spot joints.

From literature, it is observed that the research work on RSW of DP steel DP800 steel is limited. The research work so far on RSW of DP steel is mainly focused on the investigating the weldability of different grades of DP steel. The microstructural characteristcis and mechanical properties of RS welded DP steel is well reported in literature. However, less attention is given

on parametric modeling and optimization to maximize the strength performance of joints. The mathematical modeling plays a significant role in predicting the mechanical properties of joints. The literature availble work on mathematical modeling of RSW parameters and prediction of strength and nugget hardness of joints is deficient. Process parameters significantly influences the mechanical properties of joints and can be well established using response surface methodology (RSM). The direct and interaction effect of RSW paraemters on mechanical properties of DP 800 steel is deficient. So the main objective of this investigation is to analyze the direct and interaction effect of RSW parameters on strength and nugget hardness of DP800 steel joints using RSM.

EXPERIMENTAL METHODOLOGY

Material and specimen preparation

Cold-rolled steel sheets of DP 800 steel with a thickness of 1.6 mm are employed for the optimization study of RSW parameters. The chemical composition of base metal is shown in Table 1. Table 2 shows the mechanical properties of base metal.

Table 1 *chemical composition (wt.%) of DP800 steel*

C	Si	Mn	Cr	P	S	Ni	Mo	Ti	Fe
0.146	0.88	1.500	0.025	0.007	0.0036	0.027	0.0018	0.0016	balance

Table 2*. Mechanical properties of DP800 steel*

0.2% offset Yield Strength (MPa)	Ultimate Tensile Strength (MPa)	Elongation in 50 mm gauge length (%)	Microhardness (HV)
604	832	26	295

The sheets were obtained in the size of 300 x 300 x 3 mm. The sheets were sliced to make the tensile shear fracture load (TSFL) specimens. Figure 1 shows the dimensions of STRAIGHT-TSFL and CROSS-TSFL specimens.

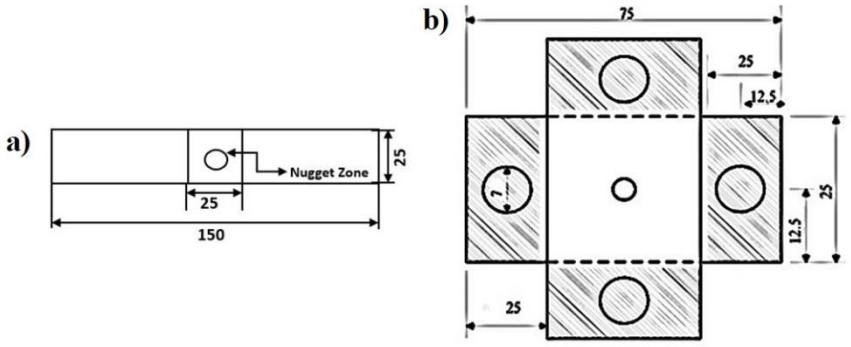


Fig. 1. Dimension of TSFL specimens: a) STRAIGHT-TSFL and b) CROSS-TSFL

Identification of RSW parameters

As illustrated in Figure 2, a semi-automatic RSW machine was used to join DP800 steel sheets. The welding current (WC), electrode pressure (EP), and welding time (WT) is found to be the most significant input parameters influencing the nugget formation, microstructural features, and strength of DP800 steel joints in the earlier investigations. Response surface methodology (RSM) is commonly employed for optimizing process parameters. It is a set of mathematical equations used to develop a design matrix for predicting the responses [23-25]. RSM is also utilized to fit the empirical relationships to data obtained from the developed design matrix. The main idea of RSM is to develop an experimental design to attain an optimal condition of process parameters [26, 27]. It is feasible to examine the interaction effect of process parameters on joint features and identify an optimal solution to get better outcomes using RSM approach [28].



Fig. 2. Photograph of RSW machine

Developing central composite design (CCD) matrix and joints preparation

A Conical type water-cooled electrode was used with dimensions of 16 mm shank and 5 mm lid diameter. The diameter of the electrode tip was determined as 6 mm from the equation $d=4\sqrt{t}$, where t is the thickness of the plate in mm. Extensive trials with a combination of various RSW parameters were performed to determine the possible working limits for joining DP 800 steel. Figure 3 displays the cause-and-effect diagram working limits of RSW for developing the lap joints of DP 800 steel.

Table 3. *Working limits of the process parameters*

Parameter	Notation	units	Levels				
			-1.68	-1	0	+1	+1.68
Welding current	WC	kA	4.0	4.5	5.0	5.5	6.0
Electrode pressure	EP	MPa	3.5	3.75	4.0	4.25	4.5
Welding time	WT	s	0.5	1.0	1.5	2.0	2.5

The feasible limits were determined by analyzing the impact of copper electrodes formed on both the sies of steel, hot expulsion at weld spots, and visually detecting other RSW defects. Table 3 shows the three factors and five levels of RSW parameters that were utilised to create the central composite design (CCD) matrix.

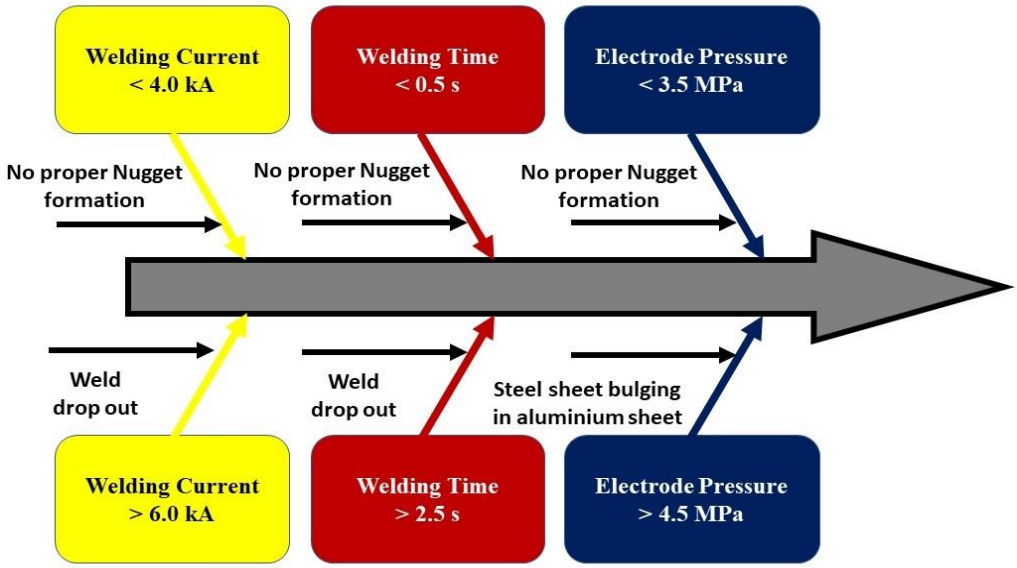


Fig. 3. Cause and effect diagram showing working limits of RSW parameters in joining DP800 steel

There are two main types of response surface designs: central composite design (CCD) and box Behnken design (BHD). In this CCD is used to design experimental matrix. A central composite design is the most commonly used response surface designed experiment. Central composite designs are a factorial or fractional factorial design with center points, augmented with a group of axial points (also called star points) that lets to estimate curvature. Central Composite designs can fit a full quadratic model. They are often used when the design plan calls for sequential experimentation because these designs can include information from a correctly planned factorial experiment. Box-Behnken designs usually have fewer design points than central composite designs, thus, they are less expensive to run with the same number of factors. They can efficiently estimate the first- and second-order coefficients; however, they can't include runs from a factorial experiment. Box-Behnken designs always have 3 levels per factor, unlike central composite designs which can have up to 5. Also unlike central composite designs, Box-Behnken designs never include runs where all factors are at their extreme setting, such as all of the low settings. Design Expert 7.0 software was used to create CCD. As shown in Table 4, it includes 20 experimental runs (2k=8 factorial points, nc=6 centre points, and 2k=6 axial points), 3 factors, and 5 levels (+/-, +/-1, and 0). Upper and lower values of RSW factors are represented by the encoded conditions -1.689 and +1.689. For lap tensile and cross tensile shear strength determination, the cut specimens were joined using RSW machine in a lap joint configuration.

Table. 4 *Design matrix of actual, coded values and their corresponding outputs*

Exp. No	Coded value			Original value			STRAIGHT -TSFL (kN)	CROSS-TSFL (kN)	NZH (HV)
	WC	EP	WT	WC (kA)	EP (MPa)	WT (s)			
1	-1	-1	-1	4.5	3.75	1.00	13.71	10.93	384
2	1	-1	-1	5.5	3.75	1.00	11.61	12.63	329
3	-1	1	-1	4.5	4.25	1.00	12.66	11.37	362
4	1	1	-1	5.5	4.25	1.00	10.3	9.94	317
5	-1	-1	1	4.5	3.75	2.00	14.78	12.4	326
6	1	-1	1	5.5	3.75	2.00	15.87	13.17	384
7	-1	1	1	4.5	4.25	2.00	10.48	11.33	330
8	1	1	1	5.5	4.25	2.00	15.97	10.97	397
9	-2	0	0	4.0	4.00	1.50	9.56	8.59	304
10	2	0	0	6.0	4.00	1.50	12.77	9.94	312
11	0	-2	0	5.0	3.50	1.50	10.67	12.33	269
12	0	2	0	5.0	4.50	1.50	12.5	10.57	261
13	0	0	-2	5.0	4.00	0.50	8.5	8	246
14	0	0	2	5.0	4.00	2.50	8.37	9.25	268
15	0	0	0	5.0	4.00	1.50	21.38	17.3	585
16	0	0	0	5.0	4.00	1.50	21.7	17.21	589
17	0	0	0	5.0	4.00	1.50	21.3	17.02	581
18	0	0	0	5.0	4.00	1.50	21.1	17.37	583
19	0	0	0	5.0	4.00	1.50	21	17.18	587
20	0	0	0	5.0	4.00	1.50	21.4	17.65	586

(Where, Welding current = WC; Electrode pressure = EP; Welding time = WT; Lap tensile shar fracture load = STRAIGHT-TSFL; Cross tensile shar fracture load = CROSS-TSFL; Nugget zone hardness = NZH)

The RSW joints of DP 800 steel were developed as per experimental runs. The photograph of as-welded RSW joints of DP 800 steel (STRAIGHT-TSFL and Cross-TSFL specimens) developed as per experimental runs are shown in Figure 4.

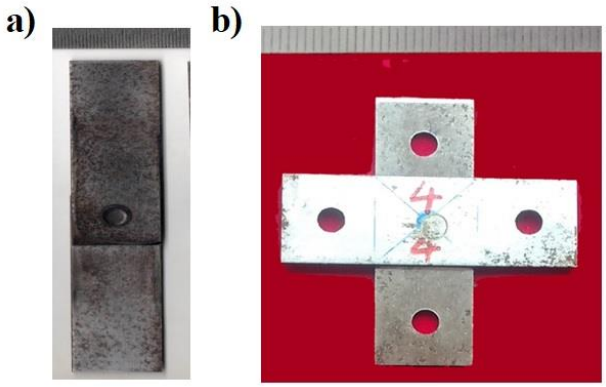


Fig. 4. Photograph of typical TSFL specimens of RSW DP800 steel joints: (a) STRAIGHT-TSFL; b) CROSS-TSFL

Tensile shear fracture load testing

To measure the TSFL of spot joints, the test specimens were created using the ASTM (E8-13) standard. A semi-automatic servo-controlled Universal testing equipment with a maximum capacity of 1000 kN was used to perform the STRAIGHT-TSFL and CROSS-TESFL tests. The as-welded TSFL specimens were loaded at 1.5 kN/min until the joint surfaces were sheared.

Three TSFL specimens were made for each welding situation, and the average of the three was reported as the final reading.

Hardness of weld nugget

On mirror-polished specimens of DP 800 steel RSW joints, the Vickers microhardness of weld nugget was measured. Vickers microhardness testing equipment was used to determine the hardness of the weld nugget cross-section with a 0.5 kg force and 15 sec dwell time.

Microstructural Characterization

For microstructural evaluation of weld nuggets, the RSW joint of DP 800 steel with the maximum strength and hardness was used. SiC abrasive paper and diamond paste were used to mount and mirror polish the cut part of the weld nugget. 1 g picric acid (C6H3N3O7), 5 ml hydrochloric acid (HCl), and 100 ml ethanol were combined to make a Villella's reagent. For 30 seconds, the mirror-polished nugget piece was etched. A stereo zoom macroscope was used to examine the macrostructural characteristics of RSW joints. Optical microscope (OM), scanning electron microscopy (SEM), and transmission electron microscope (TEM) were used to examine the microstructural properties of etched weld nugget cross sections of joints.

RESULTS AND DISCUSSION

Mathematical Model Formulation

For nugget hardness (NZH), lap tensile (STRAIGHT-TSFL), and cross tensile shear fracture load (CROSS-TSFL), a parametric mathematical equation for RSW of DP 800 steel joints was formulated. For RSW parameters, Welding current, electrode pressure, and welding duration were represented as WC, EP, and WT respectively. Nugget hardness, STRAIGHT-TSFL, and CROSS-TSFL were tested for spot joints of DP 800 steel. In equation 1, response surface for RSW joining of DP800 steel joints is provided as a function of process parameters such as WC, EP, and WT.

$$Y = f\,(WC, EP, WT) \tag{1}$$

The unknown shape of the genuine response function f, as stated in equation (1), must be calculated. When three independent RSW parameters are present, high-order polynomial regression models must be utilised. For the present prediction, RSW's 2nd order regression model was chosen above the 1st order model, which only approximates the genuine response surface in a smaller region. Multiple regression of a 2nd order response function was used to the mathematical model of RSW parameters. For the development of the response surface 'Y,' the polynomial RSW regression equation of 2nd order was used.

$$Y = b_0 + \sum b_i x_i + \sum b_{ii} x_i^2 + \sum b_{ij} x_i x_j + e_r \tag{2}$$

The polynomial equation of second order for the three-input independent RSW parameters could be represented as:

$$Y=\{ \beta_0 + \beta_1 (WC) + \beta_2 (EP) + \beta_3(WT)+\beta_{12}(WC\ X\ EP)+\beta_{13}(WC\ X\ WT)+ \beta_{23} (EP\ X\ WT) + \beta_{11} (WC)^2 + \beta_{12} (EP)^2 + \beta_{23} (WT)^2 \} \quad (3)$$

where Y = response, Xi and Xj = encoded independent variables, b_0 = mean response and bi, bii and bij = coefficients depending on linear, interaction and quadratic effects of RSW parameters.

The equations below can be used to calculate the regression coefficients for mathematical modelling of RSW.

$$b_o = 0.142857 (\sum aY)- 0.035714 \sum a \sum a (X_{ii}Y) \quad (4)$$

$$b_i = 0.041667 (\sum aX_iY) \quad (5)$$

$$b_{ii} = 0.03125 \sum a(X_{ii}Y) + 0.00372 \sum a \sum a(X_{ii}Y) – 0.035714 (\sum aY) \quad (6)$$

$$b_{ij} = 0.0625 \sum a(X_{ij}Y) \quad (7)$$

The regression coefficients of the 2nd order model for RSW joints of DP800 steel were evaluated with 95 percent confidence using the Design-Expert 7.0 software. The core RSW mathematical equations were constructed using the aforementioned equations with coefficient values. A T-test and backward elimination were used to determine the significance of RSW regression coefficients. The RSW regression coefficients and answers that were insignificant were eliminated without affecting the prediction accuracy. The RSW parametric mathematical equations were written using significant RSW coefficients. The following are the final RSW mathematical equations:

$$\text{STRAIGHT-TSFL (kN)} = - 913.57 + 9.42 (WC) + 350.27 (EP) - 10.264 (WT) - 0.086 (WC \times EP) + 0.80200 (WC \times WT) + 3.16 (EP \times WT) -0.101 (WC^2) - 43.93 (EP^2) - 13.84 (WT^2) \quad (8)$$

$$\text{CROSS-TSFL(kN)} = - 691.74 + 10.43 (WC) + 214.64 (EP) + 20.98 (WT) - 0.63 (WC \times EP) + 0.11 (WC \times WT) + 0.98 (EP \times WT) - 0.08 (WC^2) - 23.32 (WC^2) - 10 (WC^2) \quad (9)$$

$$\text{NZH (HV)} = -26058.16 + 253.26 (WC) +10067.52 (EP) + 229.3 (WT) + 1.9 (WC \times EP) + 11.25 (WC \times WT) + 51 (EP \times WT) - 2.77 (WC^2) - 1280.9 (EP^2) - 328.22 (WT^2) \quad (10)$$

Where WC = Welding current, EP = Electrode Pressure, WT = Welding Time

Proficiency verification of established RSW parametric models

Tables 5–7 provide the ANOVA findings for the data values, as well as its FIT statistics, such as adjusted R2 and projected R2 values. For adequacy verification of models in prediction and creating response surface for RSW of DP800 steel joint, the F value and p-values of RSW parametric equations were used. The relevance of RSW parametric equations is demonstrated by the F-values of 2476, 1145.47, and 7794.55 for STRAIGHT-TSFL, CROSS-TSFL, and NZH of joints. Only 0.01 percent of the time does this high "model F-value" trend as a result of noise. It suggests that RSW parameters have a considerable impact on TSFL and NZH of joints. The p-values all fall below 0.05. It highlights key RSW terms in equations. RSW parameters with p-values less than 0.1000 are considered unimportant. The most important factor determining the STRAIGHT-TSFL of joints is welding current, which is followed by welding duration and electrode pressure.

Table 5. *ANOVA test results for STRAIGHT-TSFL*

Source	Sum of Squares	df	Mean Square	F-value	p-value	
Model	512.00	9	56.89	2476.00	< 0.0001	significant
WC	11.46	1	11.46	498.70	< 0.0001	
EP	0.59	1	0.59	25.47	0.0005	
WT	3.57	1	3.57	155.47	< 0.0001	
WC X EP	0.092	1	0.092	4.02	0.0727	
WC X WT	32.16	1	32.16	1399.72	< 0.0001	
EP X WT	1.25	1	1.25	54.33	< 0.0001	
WC^2	160.73	1	160.73	6995.72	< 0.0001	
EP^2	189.58	1	189.58	8251.06	< 0.0001	
WT^2	301.16	1	301.16	13107.44	< 0.0001	
Residual	0.23	10	0.023			
Lack of Fit	0.046	5	9.152E-003	0.25	0.9235	not significant
Pure Error	0.18	5	0.037			
Cor Total	512.23	19				

Fit Statistics	Std. Dev.	0.15	R^2	0.9996
	Mean	11.29	Adjusted R^2	0.9991
	C.V. %	1.34	Predicted R^2	0.9988
			Adeq Precision	137.976

Table 6. *ANOVA test results for CROSS-TSFL*

Source	Sum of Squares	df	Mean Square	F-value	p-value	
Model	236.65	9	26.29	1145.47	< 0.0001	significant
WC	1.81	1	1.81	78.81	< 0.0001	
EP	3.10	1	3.10	134.94	< 0.0001	
WT	0.25	1	0.25	10.89	0.0080	
WC X EP	4.90	1	4.90	213.39	< 0.0001	
WC X WT	0.57	1	0.57	24.94	0.0005	
EP X WT	0.12	1	0.12	5.23	0.0453	
WC^2	100.96	1	100.96	4398.06	< 0.0001	
EP^2	53.42	1	53.42	2327.07	< 0.0001	
WT^2	157.16	1	157.16	6846.11	< 0.0001	
Residual	0.23	10	0.023			
Lack of Fit	2.073E-003	5	4.147E-004	9.115E-003	0.9856	not significant
Pure Error	0.23	5	0.045			
Cor Total	236.88	19				

Fit Statistics	Std. Dev.	0.15	R^2	0.9990
	Mean	7.52	Adjusted R^2	0.9982
	C.V. %	2.01	Predicted R^2	0.9986
			Adeq Precision	95.678

Table 7. *ANOVA test results for NZH*

Source	Sum of Squares	df	Mean Square	F-value	p-value	
Model	3.246E+005	9	36063.08	7794.55	< 0.0001	significant
WC	105.06	1	105.06	22.71	0.0008	
EP	68.06	1	68.06	14.71	0.0033	
WT	495.06	1	495.06	107.00	< 0.0001	
WC X EP	45.13	1	45.13	9.75	0.0108	
WC X WT	6328.13	1	6328.13	1367.74	< 0.0001	
EP X WT	325.13	1	325.13	70.27	< 0.0001	
WC^2	1.208E+005	1	1.208E+005	26103.26	< 0.0001	
EP^2	1.611E+005	1	1.611E+005	34828.88	< 0.0001	
WT^2	1.693E+005	1	1.693E+005	36590.83	< 0.0001	
Residual	46.27	10	4.63			
Lack of Fit	5.43	5	1.09	0.13	0.9775	not significant
Pure Error	40.83	5	8.17			
Cor Total	3.246E+005	19				

Fit Statistics	Std. Dev.	2.15	R^2	0.9999
	Mean	400.00	Adjusted R^2	0.9997
	C.V. %	0.54	Predicted R^2	0.9997
			Adeq Precision	223.116

The impact of electrode pressure on the CROSS-TSFL of joints is substantial, followed by welding current and time. Welding duration had the greatest impact on joint NZH, followed by welding current and electrode pressure. Compared to pure error, the lack of fit is not significant for STRAIGHT-TSFL, CROSS-TSFL and NZH of spot joints. The "lack of fit" values for STRAIGHT-TSFL CROSS-TSFL and NZH are of 0.9235, 0.9856 and 0.9775. In the case of RSW parametric equations. For mathematical equations of RSW, the Pred. R^2 and Adj. R^2 are in good agreement. To reach desirability, the "Adeq. Precision" refers to the signal to noise ratio, which should be greater than 4. Adeq. precision demonstrates the RSW model capability. For STRAIGHT-TSFL, CROSS-TSFL, and NZH, the precision ratios are 137.976, 95.678, and 223.116, respectively. The offered circumstances illustrate RSW parametric mathematical equations competency and their practical use in joining DP800 steel. By placing the values of RSW parameters in coded form, mathematical equations of RSW parameters may predict STRAIGHT-TSFL, CROSS-TSFL, and NZH of DP800 steel joints. A conformance test was performed on RSW mathematical models to confirm that they were consistent. Table 8 shows the percent error estimated from the experimental and anticipated values of STRAIGHT-TSFL, CROSS-TSFL, and NZH. The average error for STRAIGHT-TSFL, CROSS-TSFL, and NZH RSW equations is less than 2%. The experimental values of STRAIGHT-TSFL, CROSS-TSFL, and NZH are close to the values predicted by RSW equations, as shown in Figure 5. Thus, the RSW parametric mathematical modelling is significant and adequate for forecasting the STRAIGHT-TSFL, CROSS-TSFL, and NZH of DP800 steel RSW joints, as shown by the above results.

Table 8. *Prediction of the joint characteristics of RSW DP800 steel joints and % error*

Condition	STRAIGHT-TSFL (kN)	% Error	CROSS-TSFL (kN)	% Error	NZH ($HV_{0.5}$)	% Error
Experimental	21.70	0.60	17.65	1.78	589	0.67
Predicted	21.57		17.34		585	

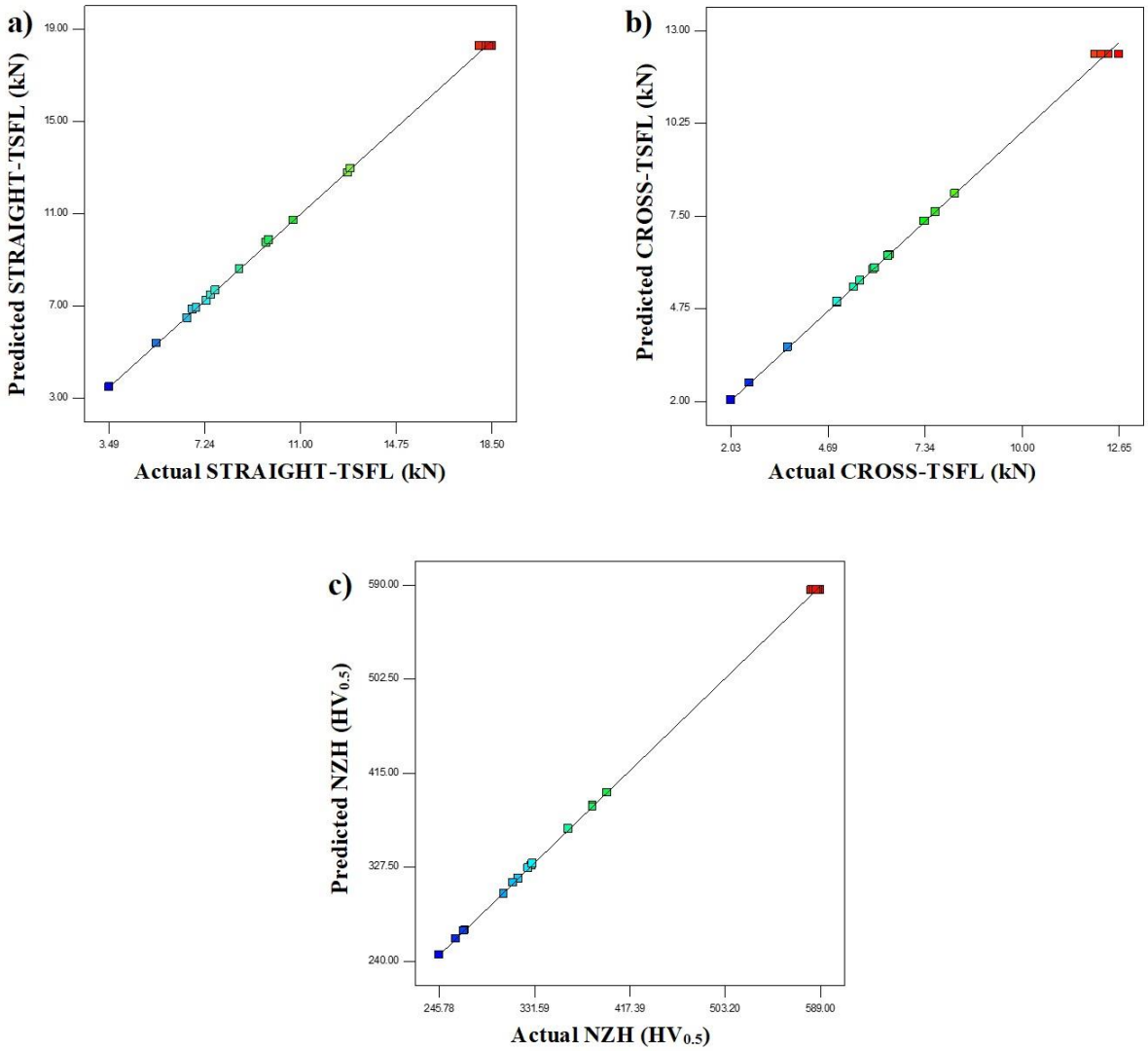


Fig. 5. Comparison of predicted and actual values: a) STRAIGHT-TSFL; b) CROSS-TSFL c) NZH of RSW DP800 steel joints

Development of 3D response surfaces for optimization of RSW parameters

RSW of DP800 steel is a multi-response issue with the goal of maximising the NZH and TSFL of spot joints. The created mathematical models were used to create 3D response surfaces that illustrate the process window and optimal region of RSW parameters to optimise the STRAIGHT-TSFL, CROSS-TSFL, and NZH of joints. The red-colored ascent part shows the highest value of TSFL and NZH of spot joints. It indicates that RSW joints of DP800 steel with a

maximum NZH of 589 $HV_{0.5}$, STRAIGHT-TSFL of 21.7 kN and CROSS-TSFL of 17.65 kN were produced with a welding current of 5.0 kA, electrode pressure of 4.0 MPa, and welding duration of 1.50 s. Table 9 shows optimal values of RSW parameters, as determined by tests and predicted by RSM. For the welding current of 5.05 kA, electrode pressure of 3.99 MPa, and welding time of 1.53 s, the maximum STRAIGHT-TSFL of 21.57 kN, CROSS-TSFL of 17.34 kN, and NZH of 585 HV0.5 were predicted for joining DP800 steel. As a result, under both experimental and prediction, the optimum RSW parameters are getting closer. Under experimental and predicted settings, the STRAIGHT-TSFL, CROSS-TSFL, and NZH of joints are also quite similar.

Table 9. *Optimized RSW parameters for joining DP800 steel*

Condition	WC (kA)	EP (MPa)	WT (s)	STRAIGHT-TSFL (kN)	CROSS-TSFL (kN)	NZH ($HV_{0.5}$)
Experimental	5.0	4.0	1.50	21.70	17.65	589
Predicted	5.05	3.99	1.53	21.57	17.34	585

Effect of RSW parameters on TSFL of DP800 steel joints

STRAIGHT-TSFL

Figure 6 a) to c) presents the 3D response surface plots for STRAIGHT-TSFL of DP800 steel joints. The maximum STRAIGHT-TSFL is displayed by the red-colored zone on response surface plots. It reveals that the STRAIGHT-TSFL is maximum at welding current of 5.0 kA, electrode pressure of 4.0 MPa, and welding time of 1.50 s. These plots also show the direct and interaction effect of any two RSW parameters considering third parameter constant. An increase in welding current from 4.0 kA to 5.0 kA increases STRAIGHT-TSFL of DP800 steel joints. Further increase in welding current above 5.0 kA causes a significant reduction in STRAIGHT-TSFL of RSW joints. It is mainly attributed to the more resistive heating of the joining surfaces. As electrode pressure increases from 3.5 MPa to 4.0 MPa, the STRAIGHT-TSFL increases. Further increase in electrode pressure above 4.0 MPa causes a significant reduction in STRAIGHT-TSFL of joints. It is mainly attributed to the thinning of the weld nugget due to the excessive electrode pressure. An increase in welding time from 0.5 s to 1.50 s causes an increase in STRAIGHT-TSFL of joints. Further, an increase in welding time to 2.5 s results in a significant reduction in STRAIGHT-TSFL of joints. It is due to the excessive resistive heating of joining surfaces.

Figure 6 a) displays the 3D response surface plot for welding current and electrode pressure considering welding time of 1.50 s. An increase in welding current and electrode pressure up to 5.0 kA and 4.0 MPa shows an increase in STRAIGHT-TSFL of joints. Further increase in welding current and electrode pressure results in a significant drop in STRAIGHT-TSFL of joints. It is attributed to the excessive resistive heating and thinning of joining surfaces at a higher level of welding current and electrode pressure. This causes increased nugget diameter leading to grain coarsening. The thinning of nugget also acts as stress concentration sites and redues the STRAIGHT-TSFL of joints.

Figure 6 b) displays the 3D response surface plot for welding current and time considering electrode pressure of 4.0 MPa. An increase in welding current and time up to 5.0 kA and 1.50 s

causes enhancement in STRAIGHT-TSFL of joints. Further, an increase in welding current and time to higher-level results in a significant reduction in STRAIGHT-TSFL of joints. It is mainly due to the excessive resistive heating of the joining surfaces. The higher heat input favours grain growth and reduces the STRAIGHT-TSFL of joints. Figure 6 c) displays the 3D response surface plot for electrode pressure and welding time considering a welding current of 4.0 kA. It shows increase in STRAIGHT-TSFL of joints up to electrode pressure of 4.0 MPa and welding time of 1.50 s. Further increase in electrode pressure and welding time leads to a reduction in STRAIGHT-TSFL of joints. It is imputed to the more resistive heating of nugget area and increased electrode pressure. The excessive deformation of highly heated nugget area leads to electrode marks on the nugget which acts as stress concentration sites during tensile loading. The increase in heat input causes grain coarsening and reduces the STRAIGHT-TSFL of joints.

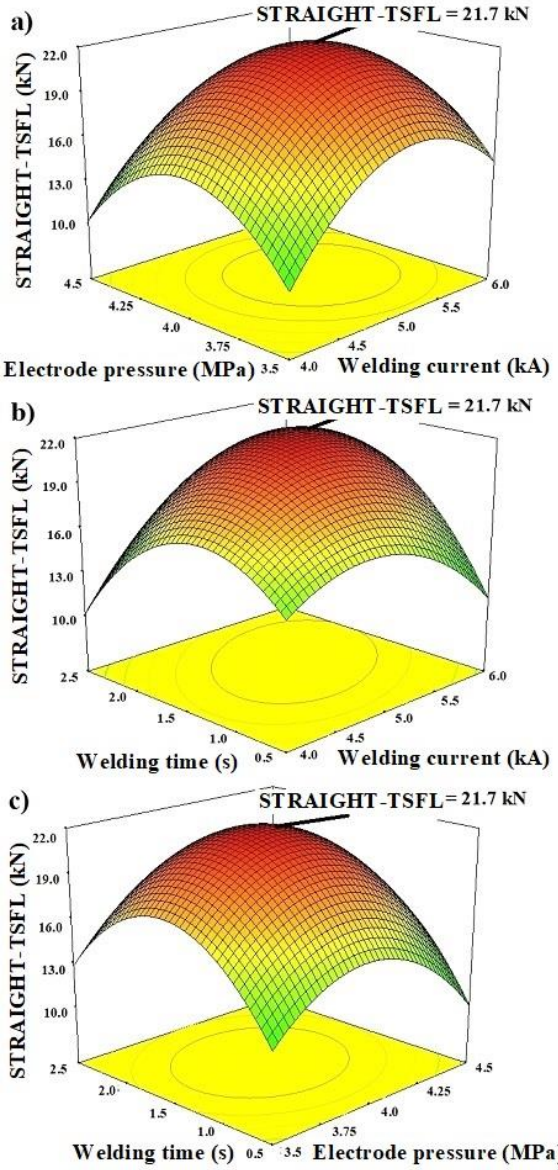


Fig. 6. 3D response surface graphs for STRAIGHT-TSFL

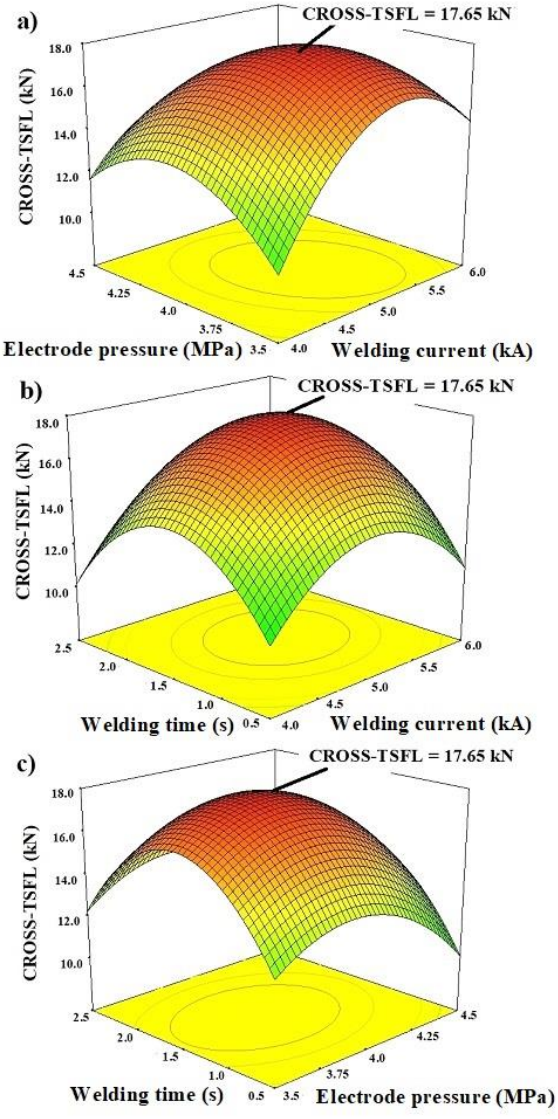


Fig. 7. 3D response surface graphs for CROSS-TSFL

CROSS-TSFL of RSW joints

Figure 7 a) to c) presents the 3D response surface plots for CROSS-TSFL of DP800 steel joints. The maximum CROSS-TSFL is displayed by the red-colored zone on response surface plots. It reveals that the CROSS-TSFL is maximum at welding current of 5.0 kA, electrode pressure of 4.0 MPa, and welding time of 1.50 s. These plots also display the direct and interaction effect of any two RSW parameters considering third parameter constant. An increase in welding current from 4.0 kA to 5.0 kA increases CROSS-TSFL of joints. Further increase in welding current above 5.0 kA causes a significant reduction in CROSS-TSFL of joints. It is mainly attributed to the more resistive heating of the joining surfaces. As electrode pressure increases from 3.50 MPa to 4.0 MPa, the CROSS-TSFL increases. Further increase in electrode pressure to 4.5 MPa causes significant reduction in CROSS-TSFL of joints. It is mainly attributed to the thinning of the weld nugget due to the excessive electrode pressure. An increase in welding time from 0.5 s to 1.50 s causes increase in CROSS-TSFL of joints. Further, increase in welding time to 2.5 s results in significant reduction in CROSS-TSFL of joints. It is due to the excessive resistive heating of joining surfaces. Figure 7 a) represents the 3D response surface plot for welding current and electrode pressure considering welding time of 1.50 s. An increase in welding current and electrode pressure up to 5.0 kA and 4.0 MPa shows increase in CROSS-TSFL of joints. Further increase in welding current and electrode pressure results in significant reduction in CROSS-TSFL of joints. It is mainly attributed to the excessive resistive heating and thinning of joining surfaces at higher levels of welding current and electrode pressure. The higher level of welding current and electrode pressure increases the nugget diameter. The larger the nugget diameter, coarser the grains. It reduces the CROSS-TSFL of joints. Figure 7 b) displays the 3D response surface plot for welding current and time considering electrode pressure of 4.0 MPa. Increase in welding current and time up to 5.0 kA a 1.50 s causes enhancement in CROSS-TSFL of RSW joints. Further, increase in welding current and time to a higher-level result in significant reduction in CROSS-TSFL of joints. It is mainly due to the excessive resistive heating of the joining surfaces. The high heat input favours the evolution of coarser grain structure and deteriorates the CROSS-TSFL of joints. Figure 7 c) displays the 3D response surface plot for electrode pressure and welding time considering welding current of 4.0 kA. It shows increase in CROSS-TSFL of joints up to electrode pressure of 4.0 MPa and welding time of 1.50 s. Further increase in electrode pressure and welding time to higher-level leads to reduction in CROSS-TSFL of joints. It is imputed to the more resistive heating of nugget and increased electrode pressure. The high heat input and excessive plastic deformation of resistively heated nugget leads to coarser grain structure and excessively deformed area acts as stress concentration site during tensile shear loading which reduces the CROSS-TSFL of joints.

NZH of RSW joints

Figure 8 a) to c) shows the 3D response surface plots for NZH of DP800 steel joints joined by RSW. The maximum NZH is disclosed by the red colored zone on response surface plots. It reveals that the RSW joints of DP800 steel made using welding current of 5.0 kA, electrode pressure of 4.0 MPa and welding time of 1.50 s exhibit higher NZH of 589 HV_{05}. It also displays the direct and interaction effect of any two RSW parameters considering third parameter constant. An increase in welding current from 4.0 kA to 5.0 kA results in increase in NZH of joints. Further increase in welding current above 5.0 kA causes significant reduction in NZH of joints. It is mainly attributed to the more resistive heating of the joining surfaces. As electrode pressure increases from 3.5 MPa to 4.0 MPa, the NZH increases. Further increase in electrode

pressure above 4.0 MPa causes significant reduction in NZH of joints. It is mainly attributed to the thinning of the weld nugget due to the excessive electrode pressure. An increase in welding time from 0.5 s to 1.50 s causes increase in NZH of joints. Further, increase in welding time to 2.5 s results in significant reduction in NZH of joints. It is due to the excessive heating of joining surfaces.

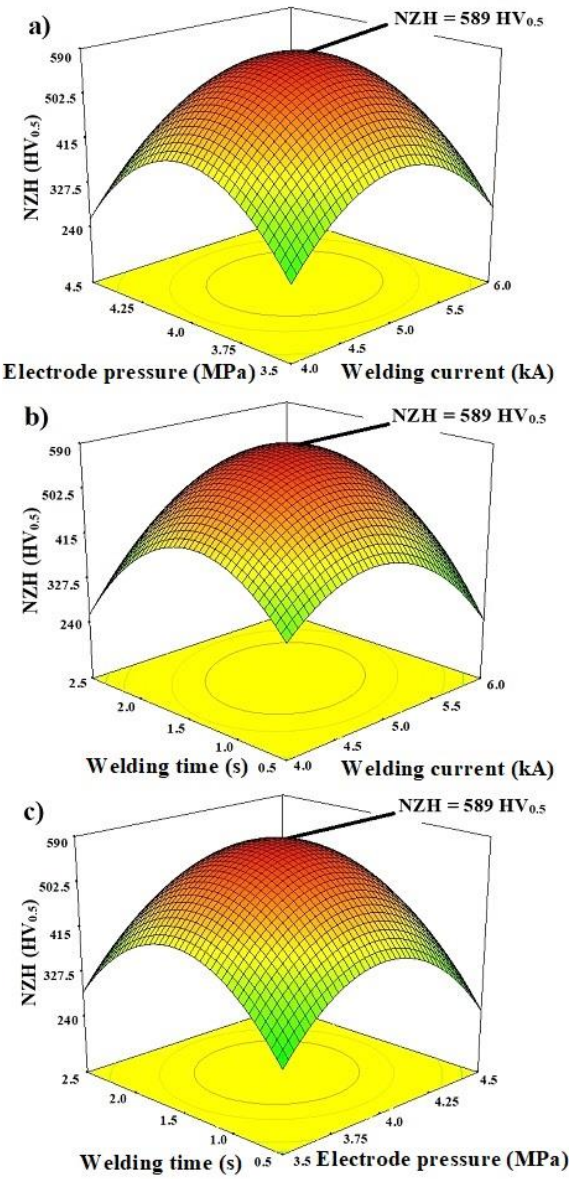


Fig. 8. 3D response surface graphs for NZH

Figure 8 a) shows the 3D response surface plot for welding current and electrode pressure considering welding time of 1.50 s. An increase in welding current and electrode pressure up to 5.0 kA and 4.0 MPa shows increase in NZH of joints. Further increase in welding current and electrode pressure results in significant reduction in NZH of joints. It is mainly attributed to the excessive resistive heating and thinning of joining surfaces at higher level of welding current and

electrode pressure. The increase in heat input and excesive heating increases the nugget diameter which leads to coarsening of grains and reduces the NGH of joints. Figure 8 b) displays the 3D response surface plot for welding current and time considering electrode pressure of 4.0 MPa. Increase in welding current and time up to 5.0 kA an 1.50 s causes enhancement in NZH of RSW joints. Further, increase in welding current and time to a higher-level result in significant reduction in NZH of joints. It is mainly due to the excessive resistive heating of the joining surfaces. The excessive heating of joining surfaces increases the nugget diameter. It leads to grain coarsening and reduces the NGH of joints. Figure 8 c) displays the 3D response surface plot for electrode pressure and welding time considering welding current of 4.0 kA. It shows increase in NZH of joints up to electrode pressure of 4.0 MPa and welding time of 1.50 s. Further increase in electrode pressure and welding time to higher level leads to reduction in NZH of joints. It is imputed to the more resistive heating of nugget area and increased electrode pressure. The excessive plastic deformation and resistive heating of weld nugget area of DP800 steel lead to inferior NZH of RSW joints. The increased nugget diameter at increased levels of electrode pressure and welding time increases the grain coarsening and reduces NGH of joints.

Mechanical properties and microstructural characterization of optimized joint

Tensile shear strength properties

Figure 9 depicts an image of cracked STRAIGHT-TSFL and CROSS-TSFL specimens of DP800 steel joints for RSW parameter optimization. Tearing mode failure began in the HAZ of joints in STRAIGHT-TSFL specimens. The CROSS-TSFL specimens showed partially pullout type of failure mode in DP800 steel RSW joints. The joints welded using optimized RSW parameters showed maximum STRAIGHT-TSFL and CROSS-TSFL of 21.70 kN and 17.65 kN with 7% and 9% elongation respectively. The STRAIGHT-TSFL of RSW DP800 steel joints is 22.94% higher than CROSS-TSFL of joints. Thus, thew load-carrying capability of RSW DP800 steel joints is superior in straight lap joint configuration than cross lap joint configuration.



Fig. 9. Failure of optimized joint of RSW DP 800 steel:
a) STRAIGHT-TSFL and b) CROSS-TSFL specimen

The joints were observed to get failed by the failure energy of 85 kJ and 77 kJ in STRAIGHT-TSFL and CROSS-TSFL specimens respectively. The fractured surface of STRAIGHT-TSFL and CROSS-TSFL specimens was analyzed by SEM as shown in Figure 10.

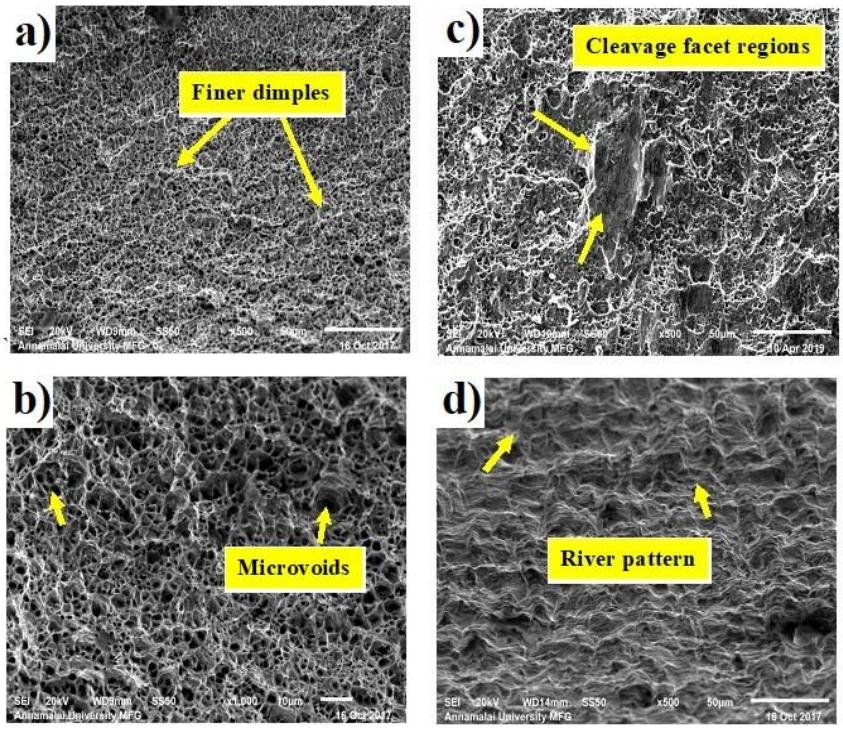


Fig. 10. SEM fractograph of TSFL specimens of optimized joint at lower and higher magnification: a) & b) STRAIGHT-TSFL; c) & d) CROSS-TSFL specimen

Due to extreme plastic deformation, the failure occurred on the weld nugget's edge. In STRAIGHT-TSFL and CROSS-TSFL specimens, the fragmented surface had finer dimpled characteristics. The size of dimples and microvoids on broken surfaces of STRAIGHT-TSFL specimens is substantially smaller, but it is somewhat coarser in CROSS-TSFL specimens. Cleavage facet areas were discovered in the CROSS-TSFL specimens. It is mainly attributed to the presence of carbides. The breakage of carbides during the tensile shear loading provides the crack imitation and propagation path resulting in the formation of cleavage facet region and river pattern.

Microhardness evaluation

The microhardness measurement was carried out across the various zones of the weldment. The microhardness of nugget zone (NZ) is directly propositional to STRAIGHT-TSFL and CROSS-TSFL. Figure 11 shows the microhardness mapping of different regions of RSW DP800 steel joints. The hardness variation was observed in nugget zone (NZ), coarse-grained HAZ (CG-HAZ), and fine grained HAZ (FG-HAZ) of welded joints. The NZ showed higher hardness than HAZ and base metal. The NZ showed higher hardness of 589 $HV_{0.5}$ which is much higher than base metal hardness of 295 $HV_{0.5}$. The harness variation was observed in HAZ of RSW joints due to change in grain size resulting in the formation of CG-HAZ and FG-HAZ. The CG-HAZ showed lower hardness than FG-HAZ owing to the grain coarsening. Due of the rapid cooling rate associated with RSW, the greater hardness of 584-589 $HV_{0.5}$ in the NZ was correlated to the development of martensite structure. Ramazani et al. [29] reported that the martensite evolution

in DP steel is approximately from 40 – 120 $^{o}Cs^{-1}$. The severe elastic strain rate during the process assisted the softening of grains in CG-HAZ and initiated failure of the spot weld.

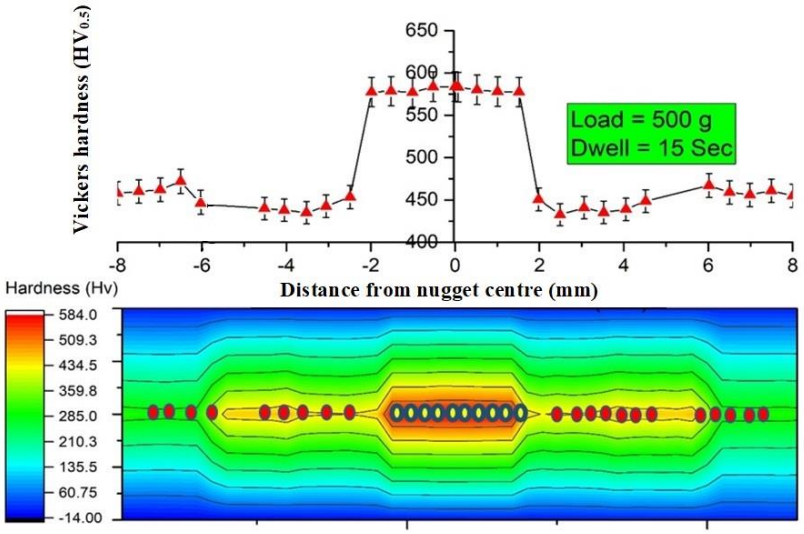


Fig. 11. Microhardness mapping of weld nugget from the centre

The hardness plot and its corresponding contour maps revealed the hardness distribution around the joints. It was evident from the distribution map that CG-HAZ regions showed less hardness when compared with FG-HAZ regions due to the fine grains associated with the latter. Due to the cooling rate of the process, the martensite formation was induced which attributed to higher hardness in NZ compared to HAZ and base metal.

Macro and microstructural characteristics

The optical microstructure of DP 800 steel base metal and different regions of spot joint is shown in Figure 12.

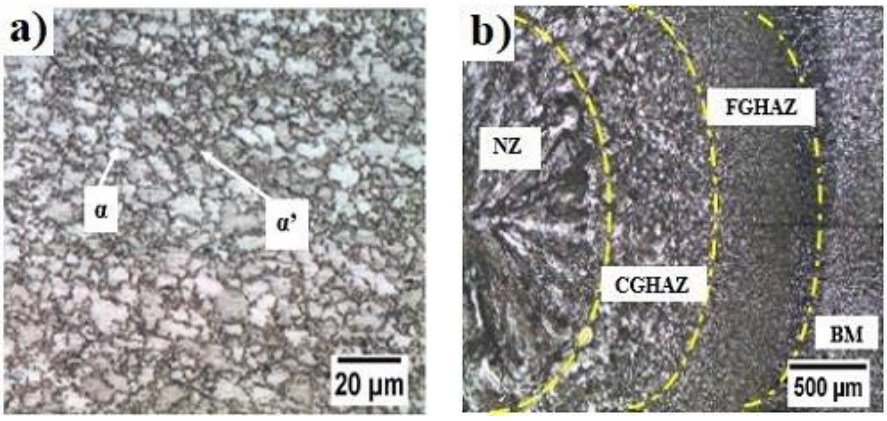


Fig. 12. a) Optical microstructure of base metal; b) weld nugget region

Along with martensite, it shows the existence of ferrite. Ferrite and martensite phases have typical grain sizes of 7-9 m and 3-7 m, respectively. The weld flaws and joint integrity were predicted by the macrostructure. The macrostructural features of the weldments were used to

examine the weld flaws and defects. Figures 13, 14 and 15 show the optical microstructures of NZ, CG-HAZ, and FG-HAZ at lower and higher magnification.

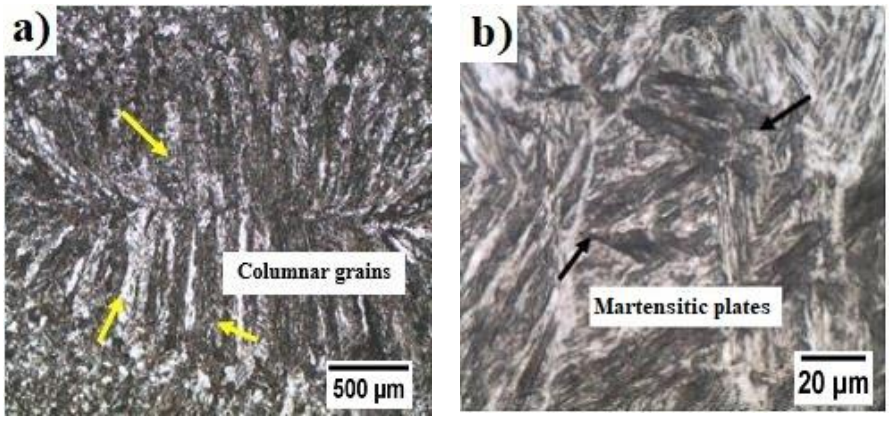


Fig. 13. Optical microstructure of nugget zone (NZ) of RSW DP800 steel joints: a) NZ at 200X; b) NZ at 500X

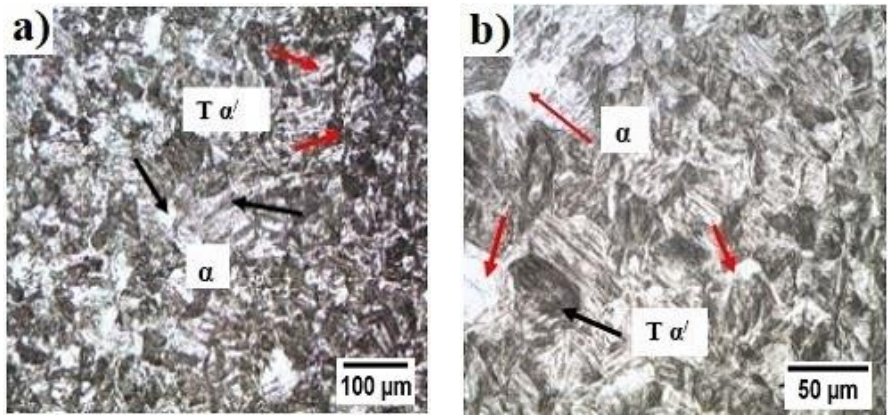


Fig. 14. Optical microstructure of coarse grain HAZ (CG-HAZ) of RSW DP800 steel joints: a) CG-HAZ at 200X; b) CG-HAZ at 500X

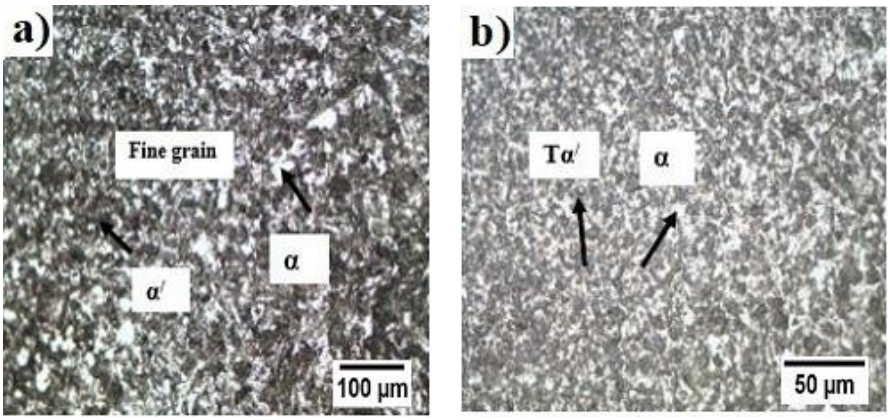


Fig. 15. Optical microstructure of fine grain HAZ (FG-HAZ) of RSW DP800 steel joints: a) FG-HAZ at 200X; b) FG-HAZ at 500X

The NZ microstructure shows dynamic recrystallization of grains exhibiting a columnar structure. This formation suggests the formation of martensite and bainite phases in the ferrite matrix during solidification [19]. The superior TSFL and NZH in optimized DP800 steel RSW

joints are attributed to the evolution of needle/lath-like martensitic structure in the nugget zone. Tempered martensite (Tα') is found in the deformed region of the CG-HAZ and FG-HAZ, with columnar/ needle/ lath type martensite (α') in the supercritical region. These phases cause the weld nugget to soften, speeding up the failure process. The region closest to the HAZ will have more elastic distortion than the surrounding areas. With a columnar shape, the average grain size of the martensite was in the range of 5–7 m. As previously noted, the grain morphology of the nugget and weld interface zones was characterised based on grain sizes and orientations in the alpha ferrite (α) matrix with columnar hard face martensite (α') and tempered martensite structure (Tα'). The evolution of these phases in the completely deformed region was assisted by the dissolution of high carbon content. The zone generated close to HAZ regions consists of ferrite and Tempered martensite (Tα') phases owing to heat dissipation. Because of the presence of soft tempered martensite (Tα'), weld failure occurred in subcritical cooling areas.

EDS and XRD anlysis of RSW DP800 steel joint

The elements in the weldment were quantified using Energy Dispersive Spectroscopy (EDS) analysis. Figure 16 illustrates the weld nugget's SEM microstructure and EDS line scan analysis.

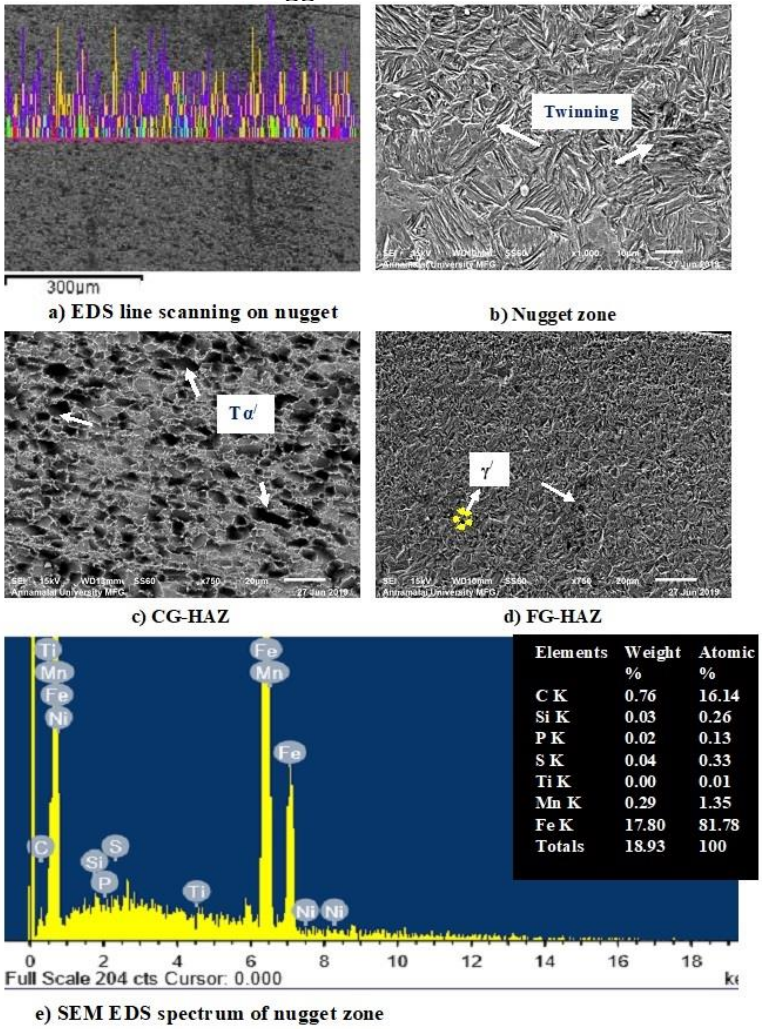


Fig. 16. SEM microstructure and EDS line scan analysis of weld nugget: a) EDS line scanning of weld nugget; b) NZ; c) CG-HAZ; d) FG-HAZ; e) SEM-EDS spectrum of NZ

Fe, Mn, C, and Si, as well as other traces, were the predominant constituents in the spot-welded zones. The phase composition of the weldments was classified using the X-ray diffraction (XRD) instrument. The atomic elements' elemental diffraction angles and intensities were used by the XRD. The peaks of the diffracted patterns may be seen as two theta angles (2θ) vs. intensity. To anticipate diffracted phases, miller indices, and D- spacing values, the XRD peaks were evaluated using pan analytical Xpert high score software. Figure 17 illustrates the XRD patterns of RSW DP800 steel joints using ODF mapping. It reveals the presence of two peak intensity phases at 45.22^{o} and 65.46^{o}, respectively, and it was functioning under the Cu-Ka1 condition (1.540598 A). Fe (45.22^{o}) and Mn (65.46^{o}) were abundant in these peak intensities, which were aided by minor elements such as Carbon and Silicon.

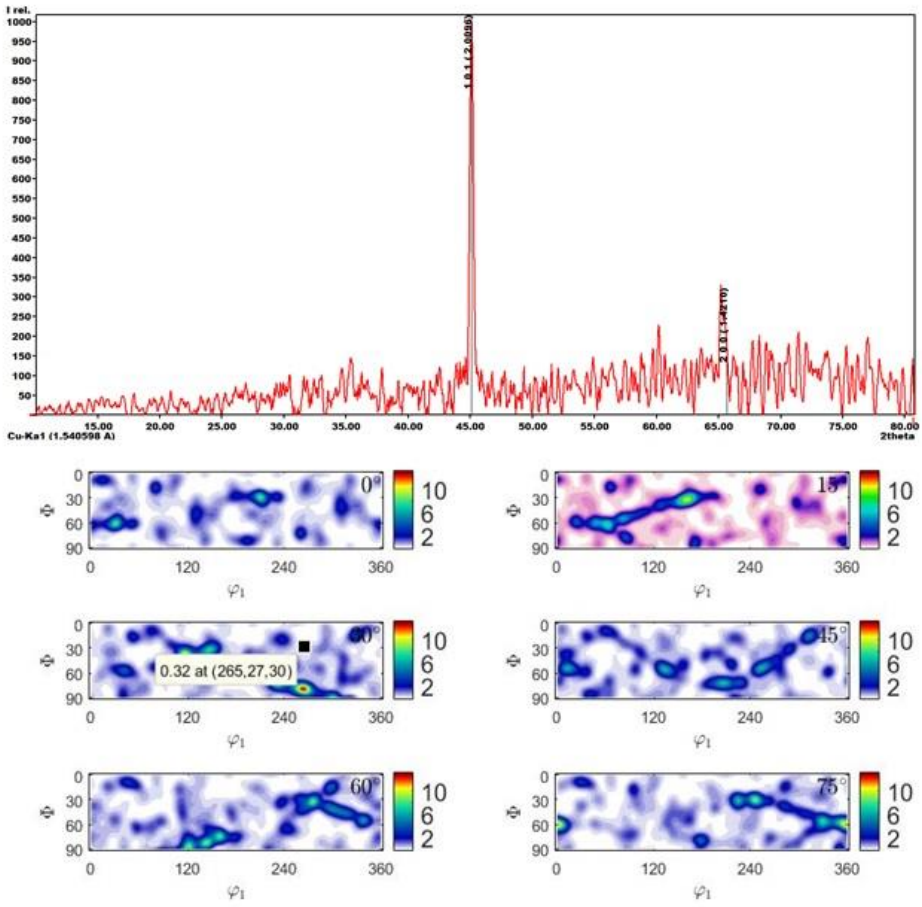


Fig. 17. XRD patterns with ODF mapping of RSW DP800 steel joints

The Fe_3C (cementite) and Mn_3C (manganese) were two potential phases detected in a nugget zone (manganese carbide). The nugget zone's critical cooling rate is primarily responsible for the evoltion of these intermetallic phases. Weld failures were mostly caused by the production of Tempered martensite (Tα') at the interfacial area of the coarser grain heat-affected zone, rather than this cementite phase. Although the miler indices and d-spacing values for iron (Fe) and manganese (Mn) rich phases were established at (101), 2.00520 Å, (200) and 1.42582 Å respectively. In addition, utilising the estimated ODF data in the diffraction, the crystal

diffraction is depicted in pole texture of Figure 17. The relationship between atomic intensity (I) and deviation angle (2θ) is established by the crystal diffraction (XRD) phenomena. The phases were identified as iron (Fe), manganese (Mn), cementite (Fe_3C), and manganese carbide based on the diffracted angles, miler indices, and d-spacing values (Mn_3C).

Microstructural analysis using TEM

Figure 18 shows the TEM microstructure of a weld nugget. Columnar/ needle/ lath type martensite structure (α') in the supercritical area of matrix is depicted in Figure 18a.

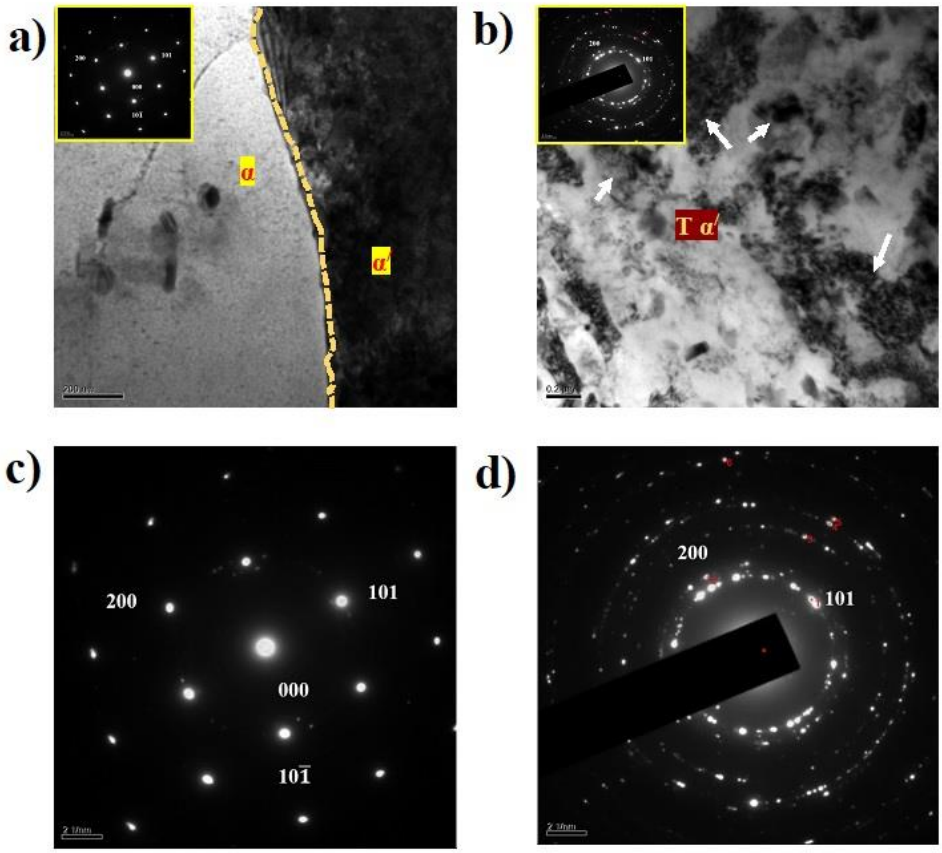


Fig. 18. TEM microstructure of nugget: a) NZ; b) HAZ; c) SAD pattern of NZ and d) SAD pattern of HAZ

Although Figure 18b depicts the sub-critical heat-affected zone (HAZ) area of dual-phase steel, the coarser grain structure is clearly visible. The distorted grain matrix comprises a few volumes of tempered martensite (Tα'). This will provide a softening effect closer to the weld joint, which is also utilised to correlate the weldment's failure pattern. Using selected area diffraction patterns to uncover crystallographic orientations (SAD). It was seen in a variety of spot weld locations, including the dynamically recrystallization region (DRX), coarser and finer grain heat impacted regions, and others (CG-HAZ & FG-HAZ). At the inner core portion, nucleated grains develop as a columnar grain, which is coupled with equiaxed grains at the outer core part. Figure 18c and d show diffracted crystallographic patterns with $[101]_{\alpha'}$ and $[200]_{\gamma}$ phases. While high cooling rates cause high carbon content in the nugget zone to dissolve, carbide phases occur [30]. Cementite (Fe_3C) and manganese carbide were discovered as

intermetallic precipitates in this diffracted pattern (Mn_3C). The cementite (η) phase has an orthorhombic crystal structure with a = 0.526 nm and c=1.263 nm lattice dimensions. Manganese (Mn) concentration stimulates the production of retained austenite interweaving in the martensitic block, according to a small number of studies [31]. It will also help to maintain the austenite phase's stability in the subcritical zone, resulting in retained austinite and tempered martensite [32]. The intermetallic precipitates Cementite (Fe_3C) and manganese carbide (Mn_3C) were discovered in the SAD patterns, and were generated as a result of the dissolution of high carbon content in the distorted areas. The cementite and manganese carbide structures were characterised as orthorhombic and body-centered cubic, respectively, with lattice dimensions of a = 0.526 nm, c=1.263 and a = 0.458 nm, c = 0.963 nm. The Fe, Mn, Si, and C elements, as well as their percentages of composition, were validated by EDS. With [101], [200] and 2.00520 Å, 1.42582 Å from XRD and 101, $\bar{1}01$, 200, $\bar{2}00$ from TEM findings, the existence of cementite and manganese carbide was verified by the diffraction pattern and SAED patterns.

CONCLUSIONS

- The 3D response surfaces were developed employing the developed mathematic models which show the process window and optimum region of RSW parameters to maximize the STRAIGHT-TSFL, CROSS-TSFL and NZH of joints. It also displays the direct and interaction effect of RSW parameters on TSFL and NZH of DP800 steel joints.
- The RSW DP800 steel joints made using welding current of 5.0 kA, electrode pressure of 4.0 MPa, and welding time of 1.50 s displayed maximum STRAIGHT-TSFL of 21.7 kN, CROSS-TSFL of 17.65 kN, and NZH of 589 $HV_{0.5}$ respectively.
- The STRAIGHT-TSFL, CROSS-TSFL and NZH of DP800 steel joints were predicted accurately with less than 2% error at 95% confidence level using the develped mathematical models of RSW.
- Welding current is the most significant parameter influencing STRAIGHT-TSFL of RSW DP800 steel joints followed by welding time and electrode pressure. The resistive heating of nugget zone offered by the welding current significantly influences the STRAIGHT-TSFL of RSW joints.
- Electrode pressure is the most significant parameter influencing the CROSS-TSFL of RSW DP800 steel joints followed by welding current and time. The plastic deformation of nugget zone offered by electrode pressure significantly influences the CROSS-TSFL of RSW joints.
- Welding time is the most significant parameter influencing the NZH of RSW DP800 steel joints followed by welding time and electrode pressure. The resistive heating offered by welding time significantly controls the cooling rate and influences the NZH of RSW joints.
- The superior joint strength and nugget zone hardness in optimized DP800 steel RSW joints is attributed to the evolution of needle/lath-like martensitic structure in the nugget zone. The weld failure occurred in the subcritical cooling regions due to the presence of soft tempered martensite ($T\alpha'$).

Acknowledgment

The authors express sincere gratitude to Director, Centre for Materials Joining and Research, CEMAJOR, Annamalai University, Annamalai Nagar, Tamil Nadu State, India for providing the resistance spot welding facility. The authors are also grateful to Alagppa University, Karaikudi for providing the materials testing facility.

REFERENCES

1. Fonstein, N.: Dual-phase steels. Automotive Steels. Woodhead Publishing (2017). https://doi.org/10.1016/B978-0-08-100638-2.00007-9
2. Mazaheri, Y.; Kermanpur A.; Najafizadeh, A.: A novel route for the development of ultrahigh strength dual phase steels. Mater Sci Eng A. 619 (2014) 1–11.
3. Li, L.: Microstructure and property control of advanced high strength automotive steels. In: Weng Y., Dong H., Gan Y. (eds) Advanced Steels. Springer, Berlin, Heidelberg, 2011.
4. Rajarajan, C.; Sivaraj, P.; Balasubramanian, V.: Microstructural characteristics and load carrying capability of resistance spot welded dual phase (DP800) steel joints. J Adv Micro Res 13 (2018) 198-203.
5. Nesterova, E.V.; Bouvier, S.; Bacroix, B.: Microstructure evolution and mechanical behavior of a high strength dual-phase steel under monotonic loading. Mater. Charact. 100 (2015) 152–162.
6. Zhang, P.; Xie, J.; Wang, Y. X.; Chen, J. Q.: Effects of welding parameters on mechanical properties and microstructure of resistance spot welded DP600 joints. Sci Technol Weld Join 16 (2011) 567-574.
7. Shome, M.; Tumuluru, M.: Welding and joining of Advanced High Strength Steels (AHSS) resistance spot welding techniques for advanced high-strength steels (AHSS). Woodhead publishing, Cambridge, UK, 2015.
8. Ambroziak, A.; Korzeniowski, M.: Using resistance spot welding for joining aluminium elements in automotive industry. Arch Civ Mech Eng. 10 (2010) 5–13.
9. Liao, X.; Wang, X.; Guo, Z.; Wang, M.; Wu, Y.; Rong, Y.: Microstructures in a resistance spot welded high strength dual phase steel. Mater Charact 61 (2010) 341–346.
10. Yuan, X.; Li, C.; Chen, J.; Li, X.; Liang, X.; Pan, X.: Resistance spot welding of dissimilar DP600 and DC54D steels. J Mater Process Technol. 239 (2017) 31–41.
11. Kishore, K.; Kumar, P.; Mukhopadhyay, G.: Insights on microstructure and failure characteristics of resistance spot welds of galvannealed dual phase steel. J Mater Eng Perform. (2022) 1-19.
12. Aydın, E.; Ertan, R. Shunting effects on the resistance spot welding parameters of DP600. Mater Test. 62 (2020) 97-103
13. Janardhan, G.; Dutta, K.; Mukhopadhyay, G. Influence of work hardening on tensile and fatigue behavior of resistance spot-welded dual-phase steel. J Mater Eng Perform. (2022) 1-14.
14. Kishore, K.; Kumar, P.; Mukhopadhyay, G.: Microstructure, tensile and fatigue behaviour of resistance spot welded zinc coated dual phase and interstitial free steel. Met Mater Inter. 28 (2022), 945-965.

15. Sevim, I.: Newly revealed features of fracture toughness behavior of spot welded dual phase steel sheets for automotive bodies. Mater Test. 57 (2015) 960-967
16. Yaghoobi, F.; Jamaati, R.; Aval, H. J.: Resistance spot welding of high-strength DP steel and nano/ultrafine-grained IF steel sheets. Mater. Chem. Phy. 281 (2022) 125909.
17. Javaheri, E.; Pittner, A.; Graf, B.; Rethmeier, M.: Mechanical properties characterization of resistance spot welded DP1000 steel under uniaxial tensile tests. Mater. Test. 61 (2019) 527-532.
18. Elitas, M.; Demir, B.; Residual stress evaluation during RSW of DP600 sheet steel. Mater. Test. 62 (2020) 888-890.
19. Marwan, K.; Kaçar, R.: Optimization of welding parameters for DP600/TRIP800 dissimilar joints. Mater Test. 60 (2018) 40-48.
20. Elitas, M.: Effects of welding parameters on tensile properties and fracture modes of resistance spot welded DP1200 steel. Mater Test. 63 (2021) 124-130.
21. Önal, A. S.; Kaya, N.: Effect and optimization of resistance spot welding parameters on the strength of welded hot-stamped parts. Mater Test. 56 (2014), 466-471.
22. Cavdar, F. Y.; Yasar, H.; Cavdar, K.: Effect of the welding parameters on the surface morphology of resistance spot welded AISI 304 stainless steel joints. Mater Test. 62 (2020) 739-743.
23. Sonar, T.; Balasubramanian, V.; Malarvizhi, S.; Venkateswaran, T.; Sivakumar, D. Development of 3-Dimensional (3D) response surfaces to maximize yield strength and elongation of InterPulsed TIG welded thin high temperature alloy sheets for jet engine applications. CIRP J Manuf Sci Technol. 31 (2020) 628-642.
24. Sonar, T.; Balasubramanian, V.; Malarvizhi, S.; Venkateswaran, T.; Sivakumar, D.: Multi-response mathematical modelling, optimization and prediction of weld bead geometry in gas tungsten constricted arc welding (GTCAW) of Inconel 718 alloy sheets for aero-engine components. Multiscale Multidiscipl Model, Exp Design, 3 (2020), 201-226.
25. Sonar, T.; Balasubramanian, V.; Malarvizhi, S.; Venkateswaran, T.; Sivakumar, D.: Maximizing strength and corrosion resistance of InterPulsed TIG welded Superalloy 718 joints by RSM for aerospace applications. CIRP J Manuf Sci Technol, 35 (2021) 474-493.
26. AnandhaKumar, C. J.; Mohan, D. G.: Predicting the ultimate tensile strength and wear rate of aluminium hybrid surface composites fabricated via friction stir processing using computational methods. J Adh Sci Technol. 36 (2022), 1707-1726.
27. Mohan, D. G.; Tomków, J.; Karganroudi, S. S.: Laser Welding of UNS S33207 Hyper-Duplex Stainless Steel to 6061 Aluminum Alloy Using High Entropy Alloy as a Filler Material. Appl Sci. 12 (2022) 2849.
28. Mohan, D. G.; Gopi, S.: Optimized parameters prediction for single-pass friction stir welding on dissimilar aluminium alloys T-joint. Inter J Emer Technol 12 (2021).
29. Ramazani, A.; Mukherjee, K.; Abdurakhmanov, A.; Abbasi, M.; Prahl, U.; Characterization of microstructure and mechanical properties of resistance spot welded DP600 steel. Met. 5 (2015) 1704–1716.
30. Kishore K.; Kumar, P.; Mukhopadhyay, G.: Resistance spot weldability of galvannealed and bare DP600 steel. J Mater Process Technol. 271 (2019) 237–248.
31. Aslanlar, S.; Ogur, A.; Ozsarac, U.; Ilhan, E.: Welding time effect on mechanical properties of automotive sheets in electrical resistance spot welding. Mater. Des. 29 (2008) 1427–1431.

32. Baltazar Hernandez, V. H.; Panda, S. K.; Okita, Y.; Zhou, N. Y.: A study on heat affected zone softening in resistance spot welded dual phase steel by nanoindentation. J Mater Sci. 45 (2010) 1638–1647.